The Astrophysical Journal Letters, 969:L8 (7pp), 2024 July 1 https://doi.org/10.3847/2041-8213/ad527b

A JWST Project on 47 Tucanae: NIRSpec Spectroscopy of Multiple Populations among M Dwarfs*

A. F. Marino[1], A. P. Milone[1,2], A. Renzini[1], E. Dondoglio[1], E. Bortolan[2], M. G. Carlos[3], G. Cordoni[4], A. Dotter[5], S. Jang[6], E. P. Lagioia[7], M. V. Legnardi[2], F. Muratore[2], A. Mohandasan[2], M. Tailo[1], and T. Ziliotto[2]
[1] Istituto Nazionale di Astrofisica—Osservatorio Astronomico di Padova, Vicolo dell'Osservatorio 5, Padova, IT-35122, Italy; anna.marino@inaf.it
[2] Dipartimento di Fisica e Astronomia "Galileo Galilei"—Univ. di Padova, Vicolo dell'Osservatorio 3, Padova, IT-35122, Italy
[3] Theoretical Astrophysics, Department of Physics and Astronomy, Uppsala University, Box 516, SE-751 20 Uppsala, Sweden
[4] Research School of Astronomy and Astrophysics, Australian National University, Canberra, ACT 2611, Australia
[5] Department of Physics and Astronomy, Dartmouth College, 6127 Wilder Laboratory, Hanover, NH 03755, USA
[6] Center for Galaxy Evolution Research and Department of Astronomy, Yonsei University, Seoul 03722, Republic of Korea
[7] South-Western Institute for Astronomy Research, Yunnan University, Kunming 650500, People's Republic of China
Received 2024 April 12; revised 2024 May 29; accepted 2024 May 30; published 2024 June 24

Abstract

We present the first spectroscopic estimates of the chemical abundance of M dwarf stars in a globular cluster (GC), namely 47 Tucanae. By exploiting NIRSpec on board the James Webb Space Telescope, we gathered low-resolution spectra for 28 stars with masses in the range ∼0.4–0.5 $M_{\odot}$. The spectra are strongly affected by the H_2O water vapor bands, which can be used as indicators of oxygen abundance. The spectral analysis reveals that the target stars feature a different O abundance, with a difference of ∼0.40 dex between the first and the most polluted second population. The observed range is similar to that observed among red giant stars. This result reinforces previous findings based on the analysis of photometric diagrams, including the "chromosome maps," providing a first, and more direct, evidence of light element variations in the M dwarfs' mass regime. The observation that the multiple populations, with their variations in light elements, exhibit the same patterns from the lower main sequence all the way to the red giant branch further strengthens the notion that multiple stellar populations in GCs formed in a series of bursts of star formation.

Unified Astronomy Thesaurus concepts: Globular star clusters (656)

1. Introduction

As vividly illustrated by data from the Hubble Space Telescope (HST), globular clusters (GCs) harbor multiple sequences along the color–magnitude diagram (CMD), from below the main-sequence turnoff all the way to the red giant branch (RGB) and the asymptotic giant branch (e.g., Piotto et al. 2015; Milone et al. 2015, 2017a). Multiband HST imaging from the UV to optical has been instrumental in producing a detailed taxonomy of the multiple population phenomenon in GCs, thanks to different OH, NH, and CN molecular blanketing due to different abundances of these elements in the various populations in each cluster. Direct spectroscopy of photometrically selected stars belonging to different populations has further validated the interpretation of the photometric classification (Marino et al. 2019).

This exquisite data set has allowed us to constrain the detailed properties of the multiple population phenomenon. In brief, we know that at least two populations (first, 1P, and second, 2P, population) can be distinguished in all the analyzed GCs, with several of them showing multiple 2P components. Thus, 1P stars have chemical abundances similar to Halo field stars of the same metallicity ([Fe/H]), 2P stars are instead O- and C-depleted to various degrees, and enhanced in the products of the H-burning at high temperatures, such as He, N, Na, and Al (e.g., Gratton et al. 2004; Marino et al. 2019).

The multiple population phenomenon has been interpreted in terms of successive stellar generations, i.e., multiple bursts of star formation taking place within the forming GC while the chemical composition of its interstellar medium was (rapidly) evolving as a consequence of pollution from evolved 1P stars. In this scenario, the observed predominance of the 2P component, contributing more than half the mass of today's GCs (Milone et al. 2017a), is a challenge, as only a small fraction of the initial 1P mass is delivered with the composition required to form 2P stars. This is known as the "mass budget problem." A way out from this is to postulate that the GC progenitors were substantially more massive and lost at least 80%–90% of their 1P mass into the Halo before delivering the naked present-day GCs (Decressin et al. 2007; D'Ercole et al. 2008; Ventura & D'Antona 2009; de Mink et al. 2009; Denissenkov & Hartwick 2014). One way of achieving this has been recently proposed in which the host (dwarf) galaxy harbors extended star formation around the nascent GC, hence the original 1P stars are distributed over a much larger volume than the GC itself (Renzini et al. 2022). Subsequent evolution and tidal interaction will then result in removing most of the original 1P stars, as indicated by *N*-body simulations (Lacchin et al. 2024).

An alternative scenario assumes that stellar populations are coeval and the chemical variations are due to mass accreted onto existing low-mass stars, rather than being the product of different episodes of star formation (Bastian et al. 2013). A fascinating development of this scenario has been proposed by

* The JWST data presented in this article were obtained from the Mikulski Archive for Space Telescopes (MAST) at the Space Telescope Science Institute. The specific observations analyzed can be accessed via doi:10.17909/6t82-4360.

Gieles et al. (2018), who suggested that 2P stars form by accretion of the material from extremely massive stars, which can form in the dense environment of a proto-GC. In this scenario, there is no need for proto-GCs to be significantly more massive than today.

Constraining the original mass of GCs is crucial to assess what the contribution of GC progenitors was to the assembly of the Milky Way halo. Moreover, depending on their mass, these stellar systems might have substantially contributed to the cosmic reionization (Katz & Ricotti 2013; Renzini 2017). All this, however, remains to be quantitatively assessed, with high-redshift observations of nascent GCs starting to provide direct critical evidence on the formation process (Vanzella et al. 2016, 2020; Adamo et al. 2024).

Due to the observational limits imposed by the instrumentation, our knowledge about the chemical abundance pattern of multiple populations was, for a long time, confined to the most luminous phases of the CMD, e.g., the red giant stars. As most of the stars are in fainter evolutionary stages, in the very low mass regimes, our current knowledge of the chemical composition of stars in GCs represents just the tip of the iceberg. Indeed, a way to disentangle between the available scenarios is offered by the comparison of their properties in stars with different masses. Any accretion phenomenon should result in fact in a less efficient capability of low-mass, fully convective, stars to retain material (Bondi & Hoyle 1944), which translates into less pronounced chemical variations with respect to those present in higher-mass stars. Though GC stars have low masses, a sizeable range can still be observed going from very low-mass stars approaching the H-burning limit up to 0.9 $M_{\odot}$.

The very first investigations of multiple populations among stars with masses down to $\sim$0.1 $M_{\odot}$ have been conducted with near-IR data from HST WFC3 for some GCs, including NGC 2808 (Milone et al. 2012), NGC 6121 (M 4; Milone et al. 2014) and others (Milone et al. 2017b, 2019), and a survey for several clusters was recently presented by Dondoglio et al. (2022). These analyses, entirely based on photometric diagrams combined with synthetic spectra, indicate that internal variations in chemical abundances persist all the way to very low-mass stars, and these variations are quantitatively similar to those observed among the giants in the same cluster. In practice, chemical differentiation is possible thanks to blanketing in the F160W band due to water vapor, thus tracing differences in oxygen abundance. Thus, multiple lower main sequences have been identified, which appear to come in the same proportion of the multiple sequences already identified among, e.g., the RGB stars of the same clusters. In Dondoglio et al. (2022) the present-day mass function in the explored stellar mass range was estimated for the various 1P and 2P populations, and found to be consistently the same (see also Milone et al. 2019; Scalco et al. 2024).

Now, thanks to the new facilities on board the James Webb Space Telescope (JWST), the observation of GC stars down to very faint magnitudes has become considerably more efficient than with previous telescopes. The first evidence of multiple stellar populations in very low-mass stars below the main-sequence knee has been reported for NGC 104 (47 Tucanae; Milone et al. 2023), M 92 (Ziliotto et al. 2023), and NGC 6440 (Cadelano et al. 2023), using H_2O blanketing (e.g., in the F150W, F200W, or F322W2 bands). Most recently, the CMD of 47 Tucanae from very deep JWST/NIRCam data has reached, for the first time, the H-burning limit and the more luminous brown dwarfs (Marino et al. 2024).

In this work, we take advantage of the capabilities of the JWST multiobject spectrograph NIRSpec to characterize the multiple stellar populations among the M dwarfs of this cluster. Until now, the spectroscopic observation of such faint stars was prohibitive, but JWST with NIRSpec allows us to make a big step forward in this context. We in fact have reached the faintest stars ever observed in a GC and use these data to document the multiple stellar population phenomenon in M dwarfs from *direct* spectroscopic measurements, thus providing a consistent characterization combining photometric and spectroscopic data.

The layout of this work is as follows: Section 2 presents the observations, Section 3 the analysis, and finally, Section 4 discusses the results.

2. The Data Set

We have acquired JWST data for 47 Tucanae from parallel observations, including both spectra from NIRSpec and photometric data from NIRCam (GO2560, PI: Marino). NIRSpec data were gathered by using the G235M/F170LP disperser-filter combination, which provides a 1.66–3.07 μm range in wavelength and a resolution of $R \sim 1000$. To simultaneously observe many targets, we employed the multiobject spectroscopy mode using the micro-shutter assembly (MSA) configuration. In parallel, NIRCam was observed in the two filters F115W and F322W2, those that most efficiently ensure the separation of multiple sequences among M dwarfs (Milone et al. 2023; Marino et al. 2024), again using H_2O blanketing but this time in the F322W2 passband.

Observations were gathered in 2022 July in the first JWST cycle, but they experienced technical issues. Specifically, wind-tilt events affected the quality of the data (see Milone et al. 2023 for more details), and nodding issues resulted in missing spectra in one of the two nod positions. In the end, while photometric images were analyzed anyway in Milone et al. (2023), NIRSpec data were not suited for a straightforward analysis, with only a few stars having spectra of sufficient quality.

New observations were then completed in 2023 September. We employed the same strategy as the first observations and gathered spectroscopic and photometric data in parallel. This time we did not experience any failure and obtained new images and spectra. While for the photometric analysis and the presentation of the first spectra we refer to Marino et al. (2024), here we analyze the full spectroscopic data set.

NIRSpec spectra for a sample of 29 M dwarfs were obtained in the magnitude interval $19.5 \lesssim m_{\rm F160W} \lesssim 20.3$, corresponding to stellar masses between 0.35 and 0.5 $M_{\odot}$. Our exposures were organized into 16 groups, and the NRSIRS2 was employed as a readout pattern, with a total on-target time of 47,280 s for each of the observed stars.

The exposures were subdivided into two shutter nodding positions, and a dither pattern of 100 shutters has been applied, which corresponds to 20″ in the dispersion direction. Each exposure was integrated for 1182 s. Of our 28 M dwarf targets, 17 are observed in both dither positions, resulting in a total of 40 exposures, while the remaining 12 are only in one dither position, providing half of the total exposure. The 1D extracted

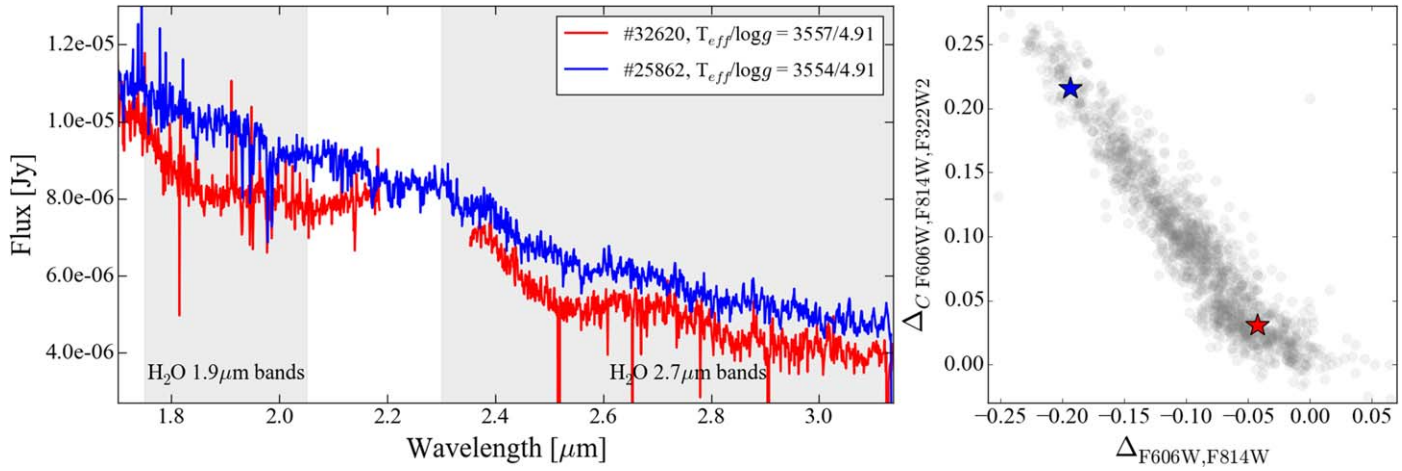

Figure 1. NIRSpec spectra for the two stars #32620 and #25862 marked with large starred symbols in the ChM from Marino et al. (2024; right panel). Based on the location on the ChM, the two stars have different values both in $\Delta_{F606W,F814W}$ and $\Delta_{C\ F606W,F814W,F322W2}$, with #32620 being a 1P star, and #25862 a 2P one. The similar values of the atmospheric parameters for the plotted stars have been reported in the inset of the left panel. The shaded regions indicate the spectral range spanned by the H_2O bands.

spectra processed with the JWST Science Calibration Pipeline (Bushouse et al. 2023) have been used for the analysis.

The location of the NIRSpec and NIRCam parallel fields are shown in Marino et al. (2024; see their Figure 1). Specifically, the NIRSpec field has pointed to the same field previously covered with HST, for which the filters F110W and F160W from GO11453 are available. The spectroscopic targets have been selected to sample the entire range in color as observed from the m_{F160W} versus $m_{F110W} - m_{F160W}$ CMD that we obtained from HST archive data. This CMD-based selection has ensured a proper sampling of all the stellar populations hosted in the cluster.

The signal-to-noise ratio of our spectra ranges from ∼60 to ∼35 per pixel, mostly depending on whether the target has been observed in both or in only one of the nod positions, respectively. An example of our spectra is shown in Figure 1, for the two stars #32620 and #25862, with very similar atmospheric parameters, log$g$ and T_{eff}. These spectra will be further discussed below, but we can already note that #32620 has much stronger H_2O molecular bands than the other. Note that this spectrum has a gap, due to the physical edges of the two detectors in the MSA, that depends on the shutter position and the disperser. Some of the gathered spectra were not analyzed because they are affected by wavelength cutoffs in crucial spectral regions for our analysis. In the spectrum of #32620, the gap is in a region not affected by the H_2O molecules, which does not prevent the analysis of this star.

3. Spectral Analysis

A visual comparison of the two spectra shown in Figure 1 (see also Figure 8 of Marino et al. 2024 for another pair of stars) clearly reveals different absorption for stars belonging to distinct stellar populations. The position of these two stars on the cluster *chromosome map* (ChM; see Milone et al. 2017a) shown in the right panel of Figure 1, suggests that #32620 is a 1P star, whereas #25862 is one of the most extremely polluted 2P stars, which we expect to be associated with the lowest oxygen abundance.

In the following, we describe our employed technique to estimate the difference in the chemical abundances of the observed M dwarfs. The spectral analysis has been conducted by comparing the observed spectra to synthetic spectra in the range from 1.5 to 2.2 μm, where the H_2O absorption is deepest.

3.1. Synthetic Spectra

The theoretical spectra have been computed by using ATLAS and SYNTHE programs[8] and α-enhanced model atmospheres with T_{eff} ranging from 3500 to 4000 K, and log g from 4.5 to 5.0, while metallicity has been set to [Fe/H] = −0.75 dex (e.g., Carretta et al. 2009a; Marino et al. 2023). The abundances of C, N, and O have been varied to mimic the chemical diversity between stars belonging to different stellar populations in GCs.[9] Spectral synthesis includes all the lines and molecules listed in the Kurucz website, including the H_2O molecular bands (Partridge & Schwenke 1997) that dominate the near-infrared (NIR) spectra of M dwarfs.

Figure 2 displays examples of the synthetic spectra with changing one-at-a-time oxygen, effective temperatures (T_{eff}), surface gravities (log g), and carbon. An inspection of these theoretical spectra immediately indicates that oxygen abundances heavily impact on the shape of the spectra, with O-enhanced stars highly absorbed all over the observed range in the wavelength (top left panel). Besides O, the next element affecting the spectra is carbon (bottom right panel), which subtracts oxygen to H_2O by locking it into CO. However, increasing [C/Fe] by 1 dex, from −1.00 to +0.00, a range often observed among different stellar populations in GCs, only marginally diminishes the overall water absorption. The impact of the other elements that are observed to vary among higher mass stars in GCs, e.g., N and Mg, is negligible in the NIR wavelength range explored here.

Together with O abundances, the effective temperature is the parameter that more heavily affects the spectra. Decreasing T_{eff} by 100 K produces a similar effect as increasing O by 0.10 dex. Instead, the effect of surface gravity is negligible.

This discussion highlights the sensitivity to O of our NIRSpec spectra of M dwarfs, which is one of the main chemical players in the multiple stellar population

[8] http://kurucz.harvard.edu

[9] Other elements, such as Na and Al, are not expected to produce changes in the overall NIRSpec spectra.

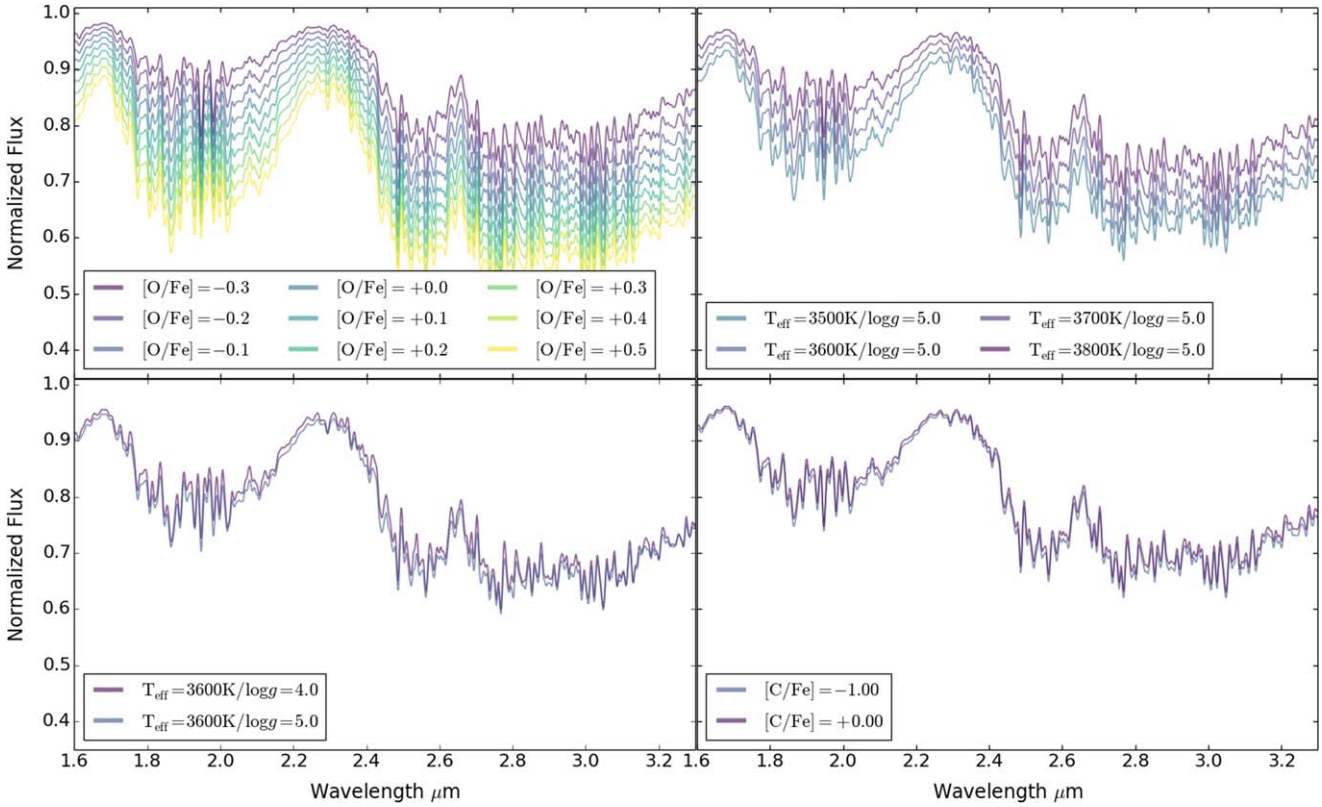

Figure 2. Synthetic spectra computed at different O abundances, keeping all the other chemical abundances and stellar parameters fixed, are shown in the top left panel. As indicated in the inset, the simulations have been computed for [O/Fe] ranging from −0.3 to +0.5 dex, with a step of 0.10 dex. The other panels illustrate the impact of changing temperatures (top right) up to 300 K (in steps of 100 K), log g by 1 dex (bottom left), and C abundances (bottom right) by 1 dex.

Table 1
Coordinates, Adopted Stellar Temperatures and Surface Gravities, Mass, Location on the Chromosome Map, and Inferred [O/Fe] Values for the NIRSpec Targets

ID	R.A. (J2000)	Decl. (J2000)	$T_{\rm eff}$ (K)	log g (cgs)	Mass ($M_\odot$)	$\Delta_{\rm F606W,F814W}$ (mag)	$\Delta_{C\ \rm F606W,F814W,F322W2}$ (mag)	[O/Fe] (dex)
3001	5.63973525	−72.09532277	3602	4.89	0.38	−0.0637	0.0368	0.29
3819	5.64094229	−72.09409725	3659	4.86	0.41	−0.1669	0.1868	0.11
8749	5.67429569	−72.08765474	3579	4.90	0.36	−0.1084	0.1005	0.29
11213	5.65667045	−72.08465712	3759	4.81	0.45	−0.0391	0.0123	0.26
12058	5.58636195	−72.08445120	3904	4.75	0.49	−0.0952	0.1070	0.30
13694	5.70320857	−72.08262859	3745	4.81	0.44	−0.1133	0.1152	0.15
14443	5.74027949	−72.08185326	3567	4.91	0.36	−0.0899	0.1214	0.25
15654	5.55751693	−72.07992265	3569	4.91	0.36	−0.1843	0.1596	−0.02
17065	5.57984182	−72.07817684	3643	4.87	0.40	−0.1270	0.1268	0.09
17470	5.59731765	−72.07867065	3785	4.79	0.46	−0.1172	0.1084	0.15
19400	5.57128890	−72.07541568	3736	4.82	0.44	−0.1455	0.1042	0.05
20051	5.72710583	−72.07569270	3788	4.79	0.46	−0.0454	0.0576	0.60
20391	5.55149616	−72.07522199	3667	4.85	0.41	−0.1917	0.1984	−0.13
20477	5.56336608	−72.07397661	3792	4.79	0.46	−0.1991	0.2330	−0.03
22777	5.68245973	−72.07146076	3668	4.85	0.41	−0.0327	0.0285	0.30
23062	5.70849703	−72.07175055	3758	4.81	0.45	−0.1803	0.2276	0.05
25260	5.59224113	−72.06959101	3618	4.88	0.38	−0.0818	0.0465	0.29
25862	5.75511193	−72.06753918	3554	4.91	0.35	−0.1934	0.2159	−0.25
32620	5.62479859	−72.06054481	3557	4.91	0.35	−0.0423	0.0311	0.42
34657	5.64627470	−72.05729149	3755	4.81	0.45	−0.0749	⋯	0.30
36425	5.64309275	−72.05518242	3902	4.75	0.49	−0.1091	⋯	0.32
37942	5.66283930	−72.05331521	3568	4.91	0.36	−0.0637	⋯	0.06
40504	5.61419155	−72.04907397	3663	4.85	0.41	−0.1150	0.1152	0.15
40579	5.65405635	−72.04884485	3713	4.83	0.43	−0.2234	⋯	−0.05
41668	5.67021510	−72.04763272	3575	4.90	0.36	−0.0998	⋯	0.05
41764	5.64695293	−72.04810886	3637	4.87	0.39	−0.0282	⋯	0.25
42484	5.63151002	−72.04646898	3821	4.78	0.47	−0.0711	⋯	0.36
48348	5.65298871	−72.03644822	3573	4.90	0.36	−0.1199	⋯	0.16

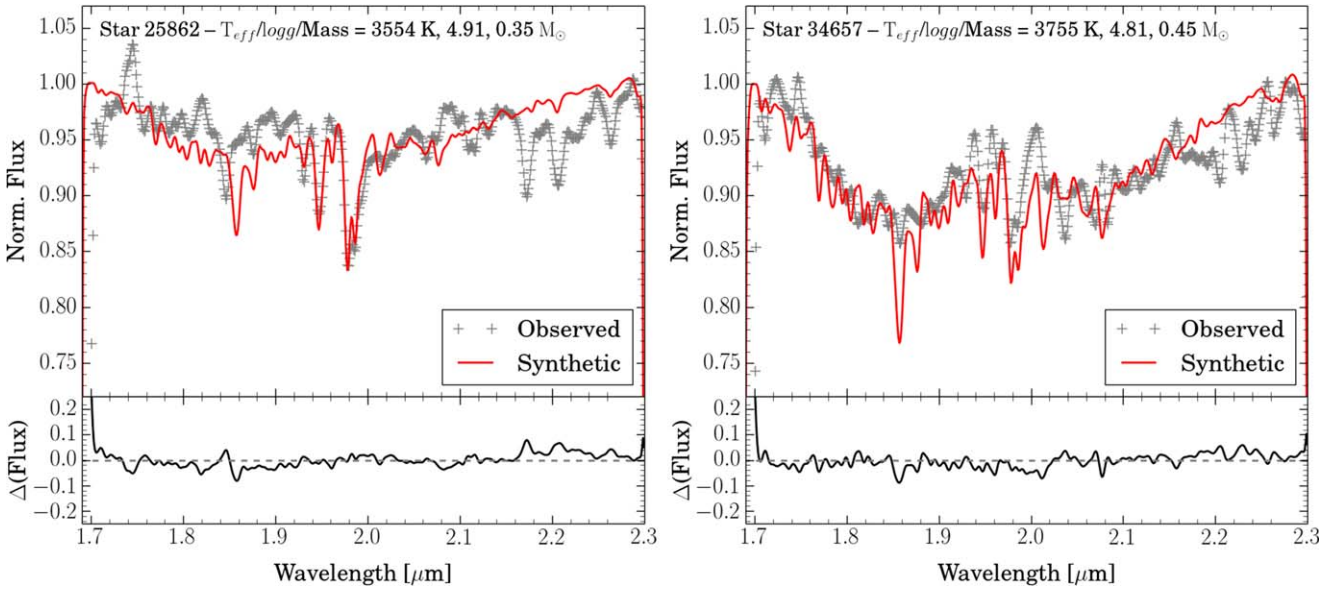

Figure 3. Examples of two spectral syntheses. The displayed observed spectra (gray crosses) are relative to stars #25862 and #34657, which have different locations on the chromosome map. Overall, the analyzed spectral regions of star #34657, photometrically classified as a 1P star, are deeper than those of #25862, which is associated with the most polluted 2P population. This is in spite of the lower temperature of the latter, which acts in the direction of deeper H_2O features (see Figure 2). The best-fit synthetic spectrum is shown in red. Both the observed and the simulated spectra have been normalized at the same pseudo-continuum, and the difference of the simulated−observed (Δ(Flux)) is shown in the bottom panels.

phenomenon. Once the $T_{\rm eff}$ is fixed, as discussed in the next section, we can proceed to estimate the O abundances from the spectra of these M dwarfs.

3.2. Observed Spectra

The observed spectra have been compared to synthetic ones with the $T_{\rm eff}/\log g$ values obtained from the position of each star on the CMD. Specifically, the $m_{\rm F814W}$ versus $m_{\rm F606W}-m_{\rm F814W}$ CMD has been fitted with α-enhanced isochrones at a metallicity $[{\rm Fe/H}] = -0.7$ dex from the Dartmouth database (Dotter et al. 2008). The distance modulus has been fixed to 13.23 mag, and reddening and age to $E(B-V) = 0.02$ mag and 12.5 Gyr, respectively. Then, we assume as $T_{\rm eff}/\log g$ for each star the values of the isochrone at the same mag level. A list of the adopted parameters, together with the estimated stellar mass, is presented in Table 1. While with this approach our estimates can be affected by systematics, we are interested here in the relative star-to-star abundance difference to infer the overall O range in these low-mass stars.

We notice here that the lower mass in our target sample is $0.35\,M_\odot$, with a total of 12 stars with mass smaller than $0.40\,M_\odot$, the approximate mass below which stars are fully convective. Hence, these stars are potentially the most important benchmarks for constraining the formation scenario of multiple stellar populations.

To compare with synthetic models, we need to normalize the observed spectra. Although the true-continuum level cannot be seen in the observed spectrum, we can exploit a pseudo-continuum. We take advantage of the two spectral regions around 1.7 and 2.3 μm, not heavily absorbed by H_2O molecules. These two regions define the edges of the spectral range used for the synthesis. The same pseudo-continuum used for the observed spectra has been assumed for the synthetic spectra. Then, we perform a χ^2 minimization to find the best-fit model. In this way, the region exploited to estimate O abundances includes the H_2O set of bands centered at 1.9 μm, which span the spectral range from 1.75 to 2.05 μm (see Figure 1). For the second band visible in our data, e.g., the H_2O band around 2.7 μm, a pseudo-continuum is much harder to define, and we prefer not to use this part of the spectrum.

Figure 3 shows some examples of the comparison between predicted and observed spectra normalized at the same pseudo-continuum. Even if the synthetic spectra do not reproduce all the observed features, probably due to the used line lists missing some features, still the overall spectral pattern is satisfactorily reproduced. Specifically, the right panel illustrates a match for a 1P star, with the best-fit synthetic spectrum having $[{\rm O/Fe}] = +0.32$ dex, while for the spectrum on the right, which belongs to a 2P star, the abundance that best matches the observations is $[{\rm O/Fe}] = -0.25$ dex. The spectrum of the O-enhanced star associated with the 1P displays much deeper H_2O band features (note that this pattern is clear even if this spectrum belongs to a star with a temperature higher than the one of the displayed 2P star, which reduces the difference due to oxygen abundances, as discussed in the previous section). The oxygen abundances inferred for the 28 analyzed M dwarfs are listed in Table 1.

As clearly shown by the synthetic spectra discussed in Section 3.1, our estimates are mostly internally affected by uncertainties in temperatures that have been fixed by isochrones. As discussed, the photometric errors suggest that the internal uncertainties in temperatures are as small as $\lesssim$50 K, which corresponds to an error in [O/Fe] of $\sim$0.05 dex. We note however that our temperatures could be affected by systematics that can be much larger than the internal errors. The overall quality of the spectra, including the limited S/N and the fitting procedure, introduce an additional random error of $\sim$0.15 dex.

Although, in general, systematic errors are expected to affect abundances uniformly, not changing the internal range in the chemical content, we discuss here possible systematics that could instead depend on the actual abundances of each star. Indeed, changes in the light element abundances, especially in helium, do impact on the adopted boundary conditions used in

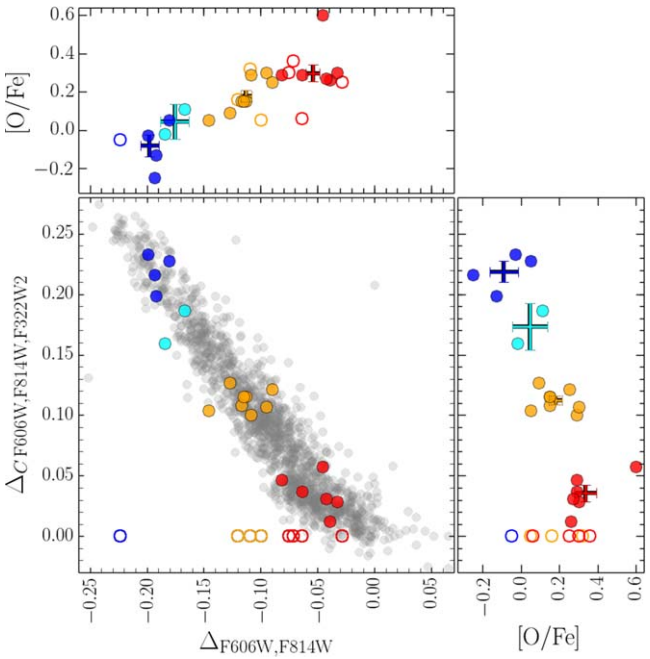

Figure 4. ChM diagram of M dwarfs in 47 Tucanae from JWST-HST photometry (gray dots). Spectroscopic targets observed with NIRSpec at JWST are represented with filled colored circles. Targets with no available m_{F322W2} from NIRCam at JWST are plotted with $\Delta_{C\ F606W,F814W,F322W2} = 0.00$ as empty circles. Different colors have been used for stars associated with different stellar populations on the ChM, specifically: first population (1P) stars are colored in red, second population ones have been colored in orange (2Pa), cyan (2Pb), and blue (2Pe). The [O/Fe] abundance vs. the $\Delta_{F606W,F814W}$ and $\Delta_{C\ F606W,F814W,F322W2}$ values are shown in the upper and right panels, respectively. For each population, we plot the average values and the associated error.

the stellar model computations, and this impacts on the predicted effective temperature scale (Pietrinferni et al. 2021; VandenBerg 2023). The average internal variation in He between 2P and 1P stars in 47 Tucanae is $\Delta(Y) = 0.011 \pm 0.005$, with a maximum variation of $\Delta(Y) = 0.049 \pm 0.005$ between the most extreme (in He enhancement/O depletion) 2P and the 1P stars (Milone et al. 2018). We have verified, by using He-enhanced isochrones, that an increase in temperature around 10 K is associated by assuming the average enhancement in He, while if we consider the most extremely He-enhanced population, the temperature rises from ∼30 for the coolest stars up to ∼50 K for the warmest ones. As previously discussed, rising temperatures systematically decrease the inferred O chemical content. However, the small variations at play only marginally change the O abundances, by at most ∼0.05 dex.

4. Results and Discussion

The comparison of the spectra illustrated in previous sections indicates the existence of a sizable spread in oxygen abundances among the M dwarfs of 47 Tucanae. Figure 4 shows the location of all the analyzed targets on the Chromosome Map (ChM) of the cluster, indicating that the whole stellar population's pattern of 47 Tucanae has been sampled by our NIRSPec spectra. We divide the ChM into four stellar populations, from the 1P (represented in red) up to the extreme population 2Pc (represented in blue), through two intermediate populations 2Pa and 2Pb (represented in orange and cyan, respectively). We can then inspect the O abundances of the selected groups.

Table 2
Average [O/Fe] Abundances, Associated Error, and rms of the Inferred for the Four Stellar Populations Selected on the M Dwarf Chromosome Map

	[O/Fe]	±	rms	#
1P	+0.30	0.04	0.13	10
2Pa	+0.18	0.03	0.09	11
2Pb	+0.04	0.09	0.09	2
2Pc	−0.08	0.06	0.13	5

Note. The number of stars (#) for each population is also indicated

From the O abundance distributions as a function of $\Delta_{F606W,F814W}$ and $\Delta_{C\ F606W,F814W,F322W2}$ plotted in Figure 4, we notice a clear trend along the ChM sequence. Specifically, there is a correlation between [O/Fe] and $\Delta_{F606W,F814W}$, and an anticorrelation with $\Delta_{C\ F606W,F814W,F322W2}$. The average abundances for each population, with relative errors determined as the rms/$\sqrt{N-1}$ (with N the number of stars in each group), are listed in Table 2. From these values, we have that the difference in the average oxygen abundance between the 1P and the population 2Pa is $\Delta([O/Fe]_{1P}–[O/Fe]_{2Pa}) = 0.12 \pm 0.05$ dex, which means at a level of $\sim 2.5\sigma$. Moving upwards in the ChM, the mean difference with the 2Pb population increases to $\Delta([O/Fe]_{1P} - [O/Fe]_{2Pb}) = +0.26 \pm 0.10$ dex, but, given that only two stars are analyzed in the 2Pb, the significance remains marginally less than 3σ. The oxygen abundance is observed to more significantly decrease in the 2Pc populations (with five [O/Fe] estimates available), with $\Delta([O/Fe]_{1P} - [O/Fe]_{2Pe}) = 0.38 \pm 0.07$ dex, a $>5\sigma$ difference. Note that also the oxygen difference between 2Pa and 2Pc is at a level of more than 3σ, e.g., $\Delta([O/Fe]_{2Pa} - [O/Fe]_{2Pe}) = 0.26 \pm 0.07$ dex. We note that the rms of each group is between ∼0.10 and ∼0.15 dex (see Table 2), which is smaller than the internal error that is estimated to be associated with the individual measurements (in Section 3.2), which might have been overestimated.

Compared to the literature values available for more massive stars, our [O/Fe] values are systematically underestimated (up to 0.15 dex), a pattern that can be expected given the diversity in the stellar parameters and the different used spectral features (Collet et al. 2007; Amarsi et al. 2016). On the other hand, the goal of this analysis is to establish the range of the oxygen abundances spanned by very low-mass stars, instead of the real abundances. In this context, we conclude that a total range of Δ[O/Fe] = 0.38 dex, found in this study, is fully consistent with the range exhibited by the red giants, as from high-resolution spectra (e.g., Carretta et al. 2009b; Dobrovolskas et al. 2014).

The presence of the same abundance variations in stars with different masses, from ∼0.8 down to ∼0.4 $M_\odot$, suggests that, in old Milky Way GCs, the multiple stellar populations phenomenon does not depend on the stellar mass. This fact represents a challenge for any accretion scenario (e.g., Bastian et al. 2013; Gieles et al. 2018) where the chemical pollution degree is expected to depend on the stellar mass. We notice that even if only a subsample of our target stars might reside below the mass limit of a fully convective regime, our results are a direct spectroscopic confirmation of that previously photometrically observed for stars fainter than the main-sequence knee, from ∼0.5 $M_\odot$ down to ∼0.1 $M_\odot$. Similar abundance patterns among today's GC main sequence, red giants, and low-mass stars down to the H-burning limit, support the scenario that the multiple stellar populations formed in different bursts of star formation.

We conclude by emphasizing that, thanks to the multiobject capabilities of NIRSpec combined with the high efficiency of the JWST in the infrared region of the spectrum, we have measured the first spectroscopic chemical abundances for M dwarfs in a GC. These observations provide the spectroscopic data of the faintest stars ever observed in these old stellar systems. Our results confirm the presence of a genuine oxygen internal spread among M dwarfs of 47 Tucanae. For the first time, the existence of a spread in light elements chemical abundances of M dwarfs has been constrained directly from spectra, confirming previous results based on photometric diagrams (Milone et al. 2012, 2014; Dondoglio et al. 2022; Milone et al. 2023; Marino et al. 2024).

Acknowledgments

We thank the anonymous referee for suggestions that improved the manuscript. This work has been funded by the European Union – NextGenerationEU RRF M4C2 1.1 (PRIN 2022 2022MMEB9W: "Understanding the formation of globular clusters with their multiple stellar generations", CUP C53D23001200006) and from INAF Research GTO-Grant Normal RSN2-1.05.12.05.10 (PI A. F. Marino) of the "Bando INAF per il Finanziamento della Ricerca Fondamentale 2022". T.Z. acknowledges support from the European Union's Horizon 2020 research and innovation program under the Marie Skodowska-Curie grant Agreement No. 101034319 and from the European Union NextGenerationEU. S.J. acknowledges support from the NRF of Korea (2022R1A2C3002992 and 2022R1A6A1A03053472).

ORCID iDs

A. F. Marino https://orcid.org/0000-0002-1276-5487
A. P. Milone https://orcid.org/0000-0001-7506-930X
A. Renzini https://orcid.org/0000-0002-7093-7355
E. Dondoglio https://orcid.org/0000-0001-8415-8531
M. G. Carlos https://orcid.org/0000-0003-1757-6666
G. Cordoni https://orcid.org/0000-0002-7690-7683
A. Dotter https://orcid.org/0000-0002-4442-5700
S. Jang https://orcid.org/0000-0002-1562-7557
E. P. Lagioia https://orcid.org/0000-0003-1713-0082
M. V. Legnardi https://orcid.org/0000-0003-3153-1499
F. Muratore https://orcid.org/0009-0003-0121-7500
A. Mohandasan https://orcid.org/0000-0001-5182-0330
M. Tailo https://orcid.org/0000-0002-1128-098X
T. Ziliotto https://orcid.org/0000-0001-8538-2068

References

Adamo, A., Bradley, L. D., Vanzella, E., et al. 2024, arXiv:2401.03224
Amarsi, A. M., Asplund, M., Collet, R., & Leenaarts, J. 2016, MNRAS, 455, 3735
Bastian, N., Lamers, H. J. G. L. M., de Mink, S. E., et al. 2013, MNRAS, 436, 2398
Bondi, H., & Hoyle, F. 1944, MNRAS, 104, 273
Bushouse, H., Eisenhamer, J., Dencheva, N., et al. 2023, JWST Calibration Pipeline, v1.10.0, Zenodo, doi:10.5281/zenodo.7795697
Cadelano, M., Pallanca, C., Dalessandro, E., et al. 2023, A&A, 679, L13
Carretta, E., Bragaglia, A., Gratton, R., D'Orazi, V., & Lucatello, S. 2009a, A&A, 508, 695
Carretta, E., Bragaglia, A., Gratton, R., & Lucatello, S. 2009b, A&A, 505, 139
Collet, R., Asplund, M., & Trampedach, R. 2007, A&A, 469, 687
de Mink, S. E., Pols, O. R., Langer, N., & Izzard, R. G. 2009, A&A, 507, L1
Decressin, T., Meynet, G., Charbonnel, C., Prantzos, N., & Ekström, S. 2007, A&A, 464, 1029
Denissenkov, P. A., & Hartwick, F. D. A. 2014, MNRAS, 437, L21
D'Ercole, A., Vesperini, E., D'Antona, F., McMillan, S. L. W., & Recchi, S. 2008, MNRAS, 391, 825
Dobrovolskas, V., Kučinskas, A., Bonifacio, P., et al. 2014, A&A, 565, A121
Dondoglio, E., Milone, A. P., Renzini, A., et al. 2022, ApJ, 927, 207
Dotter, A., Chaboyer, B., Jevremović, D., et al. 2008, ApJS, 178, 89
Gieles, M., Charbonnel, C., Krause, M. G. H., et al. 2018, MNRAS, 478, 2461
Gratton, R., Sneden, C., & Carretta, E. 2004, ARA&A, 42, 385
Katz, H., & Ricotti, M. 2013, MNRAS, 432, 3250
Lacchin, E., Mastrobuono-Battisti, A., Calura, F., et al. 2024, A&A, 681, A45
Marino, A. F., Milone, A. P., Dondoglio, E., et al. 2023, ApJ, 958, 31
Marino, A. F., Milone, A. P., Legnardi, M. V., et al. 2024, ApJ, 965, 189
Marino, A. F., Milone, A. P., Renzini, A., et al. 2019, MNRAS, 487, 3815
Milone, A. P., Marino, A. F., Bedin, L. R., et al. 2014, MNRAS, 439, 1588
Milone, A. P., Marino, A. F., Bedin, L. R., et al. 2017b, MNRAS, 469, 800
Milone, A. P., Marino, A. F., Bedin, L. R., et al. 2019, MNRAS, 484, 4046
Milone, A. P., Marino, A. F., Cassisi, S., et al. 2012, ApJL, 754, L34
Milone, A. P., Marino, A. F., Piotto, G., et al. 2015, ApJ, 808, 51
Milone, A. P., Marino, A. F., Dotter, A., et al. 2023, MNRAS, 522, 2429
Milone, A. P., Marino, A. F., Renzini, A., et al. 2018, MNRAS, 481, 5098
Milone, A. P., Piotto, G., Renzini, A., et al. 2017a, MNRAS, 464, 3636
Partridge, H., & Schwenke, D. W. 1997, JChPh, 106, 4618
Pietrinferni, A., Hidalgo, S., Cassisi, S., et al. 2021, ApJ, 908, 102
Piotto, G., Milone, A. P., Bedin, L. R., et al. 2015, AJ, 149, 91
Renzini, A. 2017, MNRAS, 469, L63
Renzini, A., Marino, A. F., & Milone, A. P. 2022, MNRAS, 513, 2111
Scalco, M., Gerasimov, R., Bedin, L. R., et al. 2024, arXiv:2403.03262
VandenBerg, D. A. 2023, MNRAS, 518, 4517
Vanzella, E., Caminha, G. B., Calura, F., et al. 2020, MNRAS, 491, 1093
Vanzella, E., de Barros, S., Vasei, K., et al. 2016, ApJ, 825, 41
Ventura, P., & D'Antona, F. 2009, A&A, 499, 835
Ziliotto, T., Milone, A., Marino, A. F., et al. 2023, ApJ, 953, 62